



137
427
THS

This is to certify that the
thesis entitled

EXPERIMENTAL INVESTIGATION INTO
EPICYCLOIDAL CENTRIFUGAL PENDULUM
VIBRATION ABSORBERS

presented by

Peter M. Schmitz

has been accepted towards fulfillment
of the requirements for the

M.S. degree in Mechanical Engineering


Major Professor's Signature

6/13/2003

Date

**EXPERIMENTAL INVESTIGATION INTO
EPICYCLOIDAL CENTRIFUGAL PENDULUM
VIBRATION ABSORBERS**

By

Peter M. Schmitz

A THESIS

Submitted to
Michigan State University
in partial fulfillment of the requirements
for the degree of

MASTER OF SCIENCE

Department of Mechanical Engineering

2003

ABSTRACT

**EXPERIMENTAL INVESTIGATION INTO
EPICYCLOIDAL CENTRIFUGAL PENDULUM
VIBRATION ABSORBERS**

By

Peter M. Schmitz

The purpose of this work is to experimentally investigate the performance of a centrifugal pendulum vibrational absorber system with the absorber constrained to move along an epicycloid path. An existing experimental facility was modified so that the behavior of either one or two absorbers could be studied. The displacements of each absorber were measured, as was the resulting angular acceleration of the rotor, for a range of torque amplitudes and orders. The results were found to be in close agreement to theoretical predictions. In addition, some instances of non-unison motion were observed and these are deserving of further theoretical investigation.

To Marcia.

ACKNOWLEDGMENTS

I cannot begin to count the number of times I wanted to give up. Each time I was convinced that there was no end in sight my advisor, Dr. Haddow, always had a remarkable way of showing that if I stay the course there will be an end. Dr. Haddow has a very contagious positive outlook on difficult problems and an overly optimistic view about finding the solution. These traits are what made working with him very enjoyable!

I would also like to thank the staff of the Physics Machine Shop for both their personal and professional advice throughout my time at MSU. Firstly for giving me the opportunity to develop a better understanding of machining practices. Secondly for giving me a job to help sustain myself financially during my two years as a graduate student. Most importantly I am deeply thankful to my boss Tom Palazzolo for setting other jobs on hold so that my project could quickly be manufactured by utilizing almost all of the human resources available. A special thanks is also extended to Jim Muns and Tom Hudson for their time and effort put towards the completion of my project.

The best kick in the butt to move on and not complain about the problems faced on my research came from my soon to be wife Marcia. She reminded me of my favorite saying that you should not complain about something if you actively do nothing about it. She has been more than understanding and made many sacrifices so that I could finish out my masters degree, and for that I am deeply grateful.

TABLE OF CONTENTS

LIST OF TABLES	vii
LIST OF FIGURES	viii
1 Introduction	1
1.1 Background of CPVAs	1
1.2 Motivation	3
1.3 Thesis Organization	4
2 CPVA Mathematical Model	5
2.1 General Information	6
2.2 Equations of Motion	7
2.3 Change of Variable and Transformation to Dimensionless Form	8
2.4 Absorber Tuning and System Resonance	10
2.4.1 Absorber Tuning	10
2.4.2 System Resonance	11
2.5 General Path Function	12
2.6 Scaling	12
2.7 Approximate Equations of Motion	13
2.8 Mistuning	14
2.9 Method of Averaging	14
2.9.1 Approximate Steady State Solutions	16
2.10 General Response for Various Path Types	16
2.10.1 Effects of Varying Torque Order on Angular Acceleration	17
2.10.2 Effects of Absorber Amplitude on Tuning Order	17
2.11 The Epicycloid Path	18
2.11.1 The Involute	20
2.11.2 The Evolute	22
3 Experimental Setup and Physical Parameters	23
3.1 Experimental Setup	23

3.1.1	Motor Control	24
3.1.2	Absorber Measuring Devices	25
3.1.3	Absorber and Rotor	27
3.1.4	Experimentally Obtained Values	28
3.2	Absorber Lengths	30
3.3	Damping	31
3.3.1	Absorber Damping Ratio	31
3.3.2	Non-dimensional Damping Factor	32
3.4	Absorber and Rotor Inertias	33
3.4.1	Total Inertia	33
3.4.2	Absorber Inertia	34
3.5	System Resonance	35
3.6	Parameter Summary	35
4	Experimental Results	37
4.1	Experimental Limitations	37
4.2	Percentage Mistuning	38
4.3	Experimental Absorber Tuning	38
4.4	Order Sweeps at Constant Values of \hat{T}_θ	40
4.4.1	One Operational Absorber	40
4.4.2	Two Operational Absorber	40
4.4.3	Discussion	41
4.5	Torque Sweeps at Constant Values of Mistuning	43
4.5.1	One Operational Absorber	43
4.5.2	Two Operational Absorber	44
4.5.3	Discussion	45
5	Conclusion	51
5.1	Future Work	52
	BIBLIOGRAPHY	54

LIST OF TABLES

3.1	Various inertias and ϵ values for different N 's.	35
3.2	System resonant orders at various number of unlocked absorbers. . .	35
3.3	Summary of physical parameters obtained experimentally.	36

LIST OF FIGURES

2.1	General CPVA Model, shown for $N=3$ absorbers.	6
2.2	Single absorber, circular path CPVA defining the parameters used in Equation 2.10.	10
2.3	Effects of varying torque order on $ \ddot{\theta} $ and absorber motion for (a) circular path absorbers (b) epicycloidal path absorbers, where $T_2=2T_1$; $T_3=2T_2$	18
2.4	Effects of torque amplitude on absorber tuning and absorber amplitude for (a) circular path absorbers (b) epicycloidal path absorbers, where $T_2=2T_1$; $T_3=2T_2$	19
2.5	Epicycloid Path.	20
2.6	Constrained path of CG following contour of the cheek with inextensible flexible bands.	21
3.1	Block diagram of experimental setup showing basic components and signal paths.	24
3.2	Close up of Absorber highlighting various parts.	26
3.3	Physical experimental setup.	27
3.4	Relationship between arc length S and absorber angle, ϕ , measured from point c in Figure 2.6.	30
3.5	Epicycloidal path compared to a circular path of radius r , both paths are tuned to same order \tilde{n}	31
3.6	Angular displacement of an absorber showing the amplitude decay as a function of time.	32
3.7	$ \ddot{\theta} $ versus \hat{T}_θ with all absorbers locked, $n=1.40$	34
4.1	Rotor angular acceleration versus applied torque order, n , at three different \hat{T}_θ values.	39
4.2	Effect of increasing order, n , at $\hat{T}_\theta = 0.198$ Nm and $\epsilon=0.07531$ with one active absorbers. (a) $ \ddot{\theta} $ of rotor, (b) absorber amplitude.	41

4.3	Effect of increasing order, n , at $\hat{T}_\theta = 0.205$ Nm and $\epsilon=0.16290$ with two active absorbers. (a) $ \ddot{\theta} $ of rotor, (b) absorber amplitude.	42
4.4	$ \ddot{\theta} $ versus \hat{T}_θ with one absorber unlocked at various levels of mistuning.	44
4.5	Absorber motion versus \hat{T}_θ with one absorber unlocked at various levels of mistuning.	45
4.6	$ \ddot{\theta} $ versus \hat{T}_θ with two absorbers unlocked at various levels of mistuning.	46
4.7	Absorber amplitudes versus \hat{T}_θ for various levels of mistuning, two absorbers unlocked.	47
4.8	Absorber response at 0% mistuning showing deviation from unison response and the average response of both absorbers.	48
4.9	Time traces for two different \hat{T}_θ values from Figure 4.8 (0% mistuning) (a) $\hat{T}_\theta=1.03$ Nm (b) $\hat{T}_\theta=1.92$ Nm.	49

NOMENCLATURE

Symbol	Description
\tilde{n}	Linearized absorber tuning order
n_2	Second resonance order
R_i	Length from center of rotation to center of gravity
r	Length from absorber pivot to absorber center of gravity
l	Length from center of rotation to absorber pivot
I_o	Inertia of all unlocked absorbers, measured from rotor's CR
J	Inertia of rotor and all locked absorbers
J_{Locked}	Total inertia of system including all locked absorbers
N	Number of absorbers unlocked
δ	Percentage of mistuning from \tilde{n}
n	Applied torque order
\hat{T}_θ	Fluctuating Torque amplitude
T_o	Constant applied torque
Ω	Mean speed of rotor
$\dot{\theta}$	Instantaneous speed of rotor
v	Dimensionless rotational speed of rotor
ϵ	Inertia ratio equivalent to b_i
b_i	inertia ratio
ζ	Absorber damping ratio

c_a	Absorber damping coefficient
$\hat{\mu}_a$	Dimensionless absorber damping
$\tilde{\mu}_a$	Scaled dimensionless absorber damping
c_o	Rotor damping coefficient
$\hat{\mu}_o$	Dimensionless rotor damping
$\tilde{\mu}_o$	Scaled dimensionless rotor damping
S	Arc length of absorber
s	Dimensionless absorber arc length
$X(S)$	General path function
$x(s)$	General dimensionless path function
σ	Mistuning parameter
$\hat{\Gamma}_\theta$	Dimensionless fluctuating torque amplitude
Γ_o	Dimensionless constant torque
m_o	Total mass of all unlocked absorber
ω_n	Natural frequency of absorber
ω_2	Second natural frequency of system
r	Averaged value of absorber amplitude
ϖ	Averaged value of absorber phase
β	Dummy parameter used for definition of involute
a	Radius of base circle for involute
b	Radius of revolving circle for involute
ϕ	Angle measured by encoder
φ	Phase angle between absorber and applied fluctuating torque

CHAPTER 1

Introduction

Torsional vibrations often arise in rotating systems because of variations in applied torques. In some situations these vibrations have detrimental effects throughout the entire system. Therefore, it is of importance to minimize these vibrations. Currently there exist a broad array of possible ways to reduce these vibrations. They range from complex active vibration control utilizing sensors and actuators, torsional dampers, increasing overall inertia, and passive type vibration absorbers. An innovative way of reducing vibrations in rotating machinery has been through the application of tuned centrifugal pendulum vibration absorbers (CPVA).

1.1 Background of CPVAs

The principle behind how a CPVA works is analogous to that of the linear translational vibration absorber. In the translational absorber it is possible to reduce vibrations of a primary mass by the introduction of a mass-spring combination tuned to the excitation frequency. This type of absorber is only effective at one particular frequency. As will be shown, the CPVA is tuned to a given order of excitation which is independent of rotational speed. A detailed analysis pertaining to the absorber tuning is provided in a later section, but in summary, a CPVA is tuned to a given

order rather than a particular excitation frequency, making the tuning of the CPVA independent of the rotational speed.

In most rotating systems, the applied fluctuating torques are generally periodic, based on the angular position, θ , of the system. For example, consider a 2 cylinder 4 stroke IC engine. Regardless of the rotational speed, each piston fires once per every other revolution of the crankshaft. Thus the system has an order, n , of 1, where the order refers to the rate at which the applied fluctuating torque repeats per revolution. It is this order that the absorbers are tuned to such that the angular acceleration is minimized.

The simplest CPVA consists of a pendulum attached to a rotor. The idea is to tune the absorber such that the absorber counteracts the applied torque by creating an opposing torque on the rotor. A further refinement to CPVAs is to choose the path that the absorber's center of gravity (CG) must follow. The path type influences how well the given CPVA performs, both in stability and general performance terms. The stability of CPVAs is an important topic, but is not discussed in detail in this dissertation (consult the works of Garg [1] and Chao [2] for further reading). Ideally, what is sought is to maximize absorber performance by utilizing a path type whose period remains constant over a large range of applied torque.

There are three path types mentioned in this dissertation, but only one will be explored in detail. Each path type has its advantages and disadvantages. The first path to consider is the circular path. This is the easiest to manufacture and implement. However, as the amplitude grows, the period of the absorber begins to change, i.e., the period of the circular path absorber is amplitude dependent. This causes the absorber to mistune at modest levels of torque due to nonlinear effects and an undesirable jump bifurcation can occur [3, 4].

The next type is the cycloidal path. This has a more desirable large amplitude performance. In a gravitational field absorbers moving along a cycloidal path have

the ideal property of constant period of motion, independent of absorber amplitude. However, when operating in a rotational field, the period is also slightly nonlinear (i.e. dependent on absorber amplitude).

The final path to consider, and the focus of this dissertation, is the epicycloidal path. It is known that in a rotational potential field, absorbers riding on epicycloid paths experience periods that are independent of absorber amplitude [5]. The disadvantage of the cycloid and epicycloid is that they are generally more complex to implement physically.

1.2 Motivation

The problem at hand is to reduce the torsional vibrations that arise in a rotating system as a result of applied periodic torques. A CPVA operating on a prescribed path has been suggested to rectify this problem. Extensive analysis has already been performed on the theoretical aspects of CPVAs for all of the paths mentioned above [1, 2, 3].

Most recently, circular path CPVAs have been studied experimentally [4]. They displayed encouraging results and supported the theory favorably. It was therefore decided to extend the investigation to study absorbers riding on epicycloid paths. To this end, an existing experiment was modified to accommodate a new absorber design.

The primary interest of this dissertation will be on the performance of the absorber system and how it varies as it is mistuned relative to the applied torque. The performance of the absorber system will be measured by two different criteria. The first criteria will be how effective the absorbers are at reducing the rotor's torsional vibration, as measured by its angular acceleration. The second criteria is the overall range of applied torque over which the absorbers can function. As will become

evident, these two criteria oppose one another.

1.3 Thesis Organization

In the next chapter the equations that govern the motion of the rotor and absorbers will be derived. These equations will then be arranged into a dimensionless form and subjected to an independent variable transformation. The method of averaging will be set up to obtain approximate solutions to the exact equations of motion. The second chapter will conclude with a general comparison between the responses at various levels of torque amplitude for circular and epicycloidal path absorbers and a discussion into the epicycloidal path.

In the third chapter the experimental setup will be introduced along with a description of what is measured and how it is converted into physical units. The physical parameters introduced in Chapter 2 will be found via experimental methods. These parameters include the absorber and rotor inertias, absorber damping ratio, absorber tuning, and system resonance order.

Chapter 4 will present the experimental results for both one and two absorber systems. The effects of varying torque order and torque amplitude will be explored. The conclusions of this dissertation will be presented in the last chapter, along with recommendations for future works.

CHAPTER 2

CPVA Mathematical Model

This chapter will serve as the theoretical basis for the dissertation. It follows from the works by Garg [1], Chao [2], and Alusuwain [3], where the general equations of motion and approximate solutions have been reported for various absorber paths.

In the subsequent sections of this chapter some assumptions will be introduced to simplify the mathematical model of the CPVA. The derivation of the equations of motion for both the absorbers and rotor will be outlined and the resulting equations will be put into a dimensionless form. The general path function for an epicycloid will be discussed and a proper scaling procedure introduced to facilitate the use of the method of averaging. Particular attention will be given to the approximate solutions for the epicycloid case proposed by Chao [2], and the derivation will be extended to allow for a mistuning between the applied torque order and the absorber tuning order. This chapter will conclude with a theoretical comparison between CPVAs with circular path absorbers and epicycloidal path absorbers and a detailed description of the geometry of the epicycloidal path.

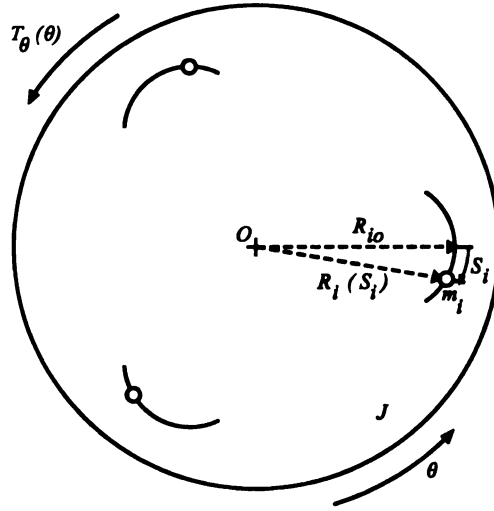


Figure 2.1. General CPVA Model, shown for $N=3$ absorbers.

2.1 General Information

The system to be studied is sketched in Figure 2.1. It consists of a rigid rotor rotating in the horizontal plane with inertia J . Attached to this rotor are N general path type absorbers each of mass m_i , whose position in the horizontal plane can be defined by a path function $R_i = R_i(S_i)$ and an arc length variable S_i . The path function is measured from the center of rotation of the rotor, O , to the center of gravity of the absorber. The arc length's origin is based at the vertex of the path function (i.e. $R_{io} = R_i(0)$). The arc length variable is also taken to be symmetrical about the vertex (i.e. $R_i(-S_i) = R_i(+S_i)$). The rotor is subjected to an applied torque of the form

$$T_\theta(\theta) = T_o + \hat{T}_\theta \sin(n\theta). \quad (2.1)$$

Where T_o is the constant applied torque necessary to counteract rotor damping, \hat{T}_θ is the amplitude of the fluctuating torque, and n is the order of the applied torque.

Not shown in Figure 2.1, but nonetheless important, is damping. The resistance

between the rotor and its pivot point at O is assumed to be viscous with a damping coefficient of c_o . Likewise there also exists damping on each of the N absorbers. Again, viscous damping is assumed with a damping coefficient for each absorber taken to be c_{ai} . It should be noted that accurately accounting for damping is very difficult since its mechanism is complex and may depend on many factors, for example material damping, friction, windage, etc. As will be shown in Section 3.3, an equivalent viscous damping coefficient is empirically found from the actual system by a standard logarithmic decrement test.

2.2 Equations of Motion

The equations of motion for the system are derived using the Lagrangian approach. The preliminary steps to derive the kinetic energy may be found in Alsuwaiyan [3], where it is shown for general paths that the kinetic energy is

$$KE = \frac{1}{2} \left\{ J\dot{\theta}^2 + \sum_{i=1}^N m_i \left[X_i(S_i)\dot{\theta}^2 + \dot{S}_i^2 + 2G_i(S_i)\dot{\theta}\dot{S}_i \right] \right\} \quad (2.2)$$

where

$$X_i(S_i) = R_i^2(S_i) \quad \text{and} \quad G_i(S_i) = \sqrt{X_i(S_i) - \frac{1}{4}\left(\frac{dX_i}{dS_i}(S_i)\right)^2}.$$

Note that $X_i(S_i)$ describes the path of the absorbers CG relative to the rotor. Various path types may be studied by specifying $X_i(S_i)$. In this dissertation, $X_i(S_i)$ will be specified in Section 2.5 such that the equations of motion will apply to a CPVA with absorbers riding on epicycloidal paths.

It should be noted that the potential energy of the system is zero since there are no energy storage devices and all motions are in the horizontal plane. However, even if the rotor was rotating in the vertical plane, the potential energy may be considered

negligible since the centrifugal force is much greater than that of gravity for any modest level of angular velocity [2]. Applying Lagrange's equations, it can be shown (see Chao [2] and Alsuwaiyan [3]) that the equations of motion for the absorbers and rotor are, respectively,

$$m_i[\ddot{S}_i + G_i(S_i)\ddot{\theta} - \frac{1}{2}\frac{dX_i}{dS_i}(S_i)\dot{\theta}^2] = -c_{ai}\dot{S}_i, \quad 1 \leq i \leq N \quad (2.3)$$

$$\begin{aligned} J\ddot{\theta} + \sum_{i=1}^N m_i \left[\frac{dX_i}{dS_i}(S_i)\dot{S}_i\dot{\theta} + X_i(S_i)\ddot{\theta} + G_i(S_i)\ddot{S}_i + \frac{dG_i}{dS_i}(S_i)\dot{S}_i^2 \right] \\ = \sum_{i=1}^N \left[c_{ai}G_i(S_i)\dot{S}_i \right] - c_o\dot{\theta} + T_o + \hat{T}_\theta \sin(n\theta). \end{aligned} \quad (2.4)$$

2.3 Change of Variable and Transformation to Dimensionless Form

Equations 2.3 and 2.4 represent a set of autonomous equations since no terms explicitly contain the independent variable t . To make these equations more amendable to further analysis, it is convenient to change the independent variable to θ , the rotor angle.

In order to accomplish this, we first redefine the rotor angular velocity in terms of a dimensionless variable v , such that

$$v \equiv \frac{\dot{\theta}}{\Omega} \quad (2.5)$$

where Ω is the mean speed of the rotor, determined by setting the fluctuating torque to zero and holding the absorbers fixed at their respective vertices. In this case

Equation 2.4 simplifies to

$$\dot{\theta} = \frac{T_o}{c_o} = \Omega. \quad (2.6)$$

Physically, this means that the constant torque T_o serves to counteract the dissipative torque from the rotor damping, which in turn sets the mean speed, Ω .

Using the new dimensionless variable, v , the derivatives with respect to t are now expressed with respect to θ using the chain rule as follows:

$$\begin{aligned} (\dot{\cdot}) &= \frac{d(\cdot)}{dt} = \Omega v(\cdot)' \\ (\ddot{\cdot}) &= \frac{d^2(\cdot)}{dt^2} = \Omega^2 v^2(\cdot)'' + \Omega^2 v v'(\cdot)' \end{aligned}$$

where $(\cdot)'$ represents $\frac{d(\cdot)}{d\theta}$.

$$\text{e.g.} \quad \ddot{\theta} = \frac{d^2\theta}{dt^2} = \Omega^2 v v'$$

The equations of motion, Equations 2.3 and 2.4, with the above substitutions become

$$v s_i'' + [s_i' + g_i(s_i)] v' - \frac{1}{2} \frac{dx_i}{ds_i}(s_i) v = -\hat{\mu}_{ai} s_i', \quad 1 \leq i \leq N \quad (2.7)$$

$$\begin{aligned} \sum_{i=1}^N b_i \left[\frac{dx_i}{ds_i}(s_i) s_i' v^2 + x_i(s_i) v v' + g_i(s_i) s_i' v v' + g_i(s_i) s_i'' v^2 + \frac{dg_i}{ds_i}(s_i) s_i'^2 v^2 \right] \\ + v v' = \sum_{i=1}^N b_i \hat{\mu}_{ai} g_i(s_i) s_i' v - \hat{\mu}_o v + \Gamma_o + \hat{\Gamma}_\theta \sin(n\theta) \end{aligned} \quad (2.8)$$

where the following dimensionless parameters have been defined

$$\left. \begin{aligned} s_i &= \frac{S_i}{R_{io}} & \hat{\mu}_o &= \frac{c_o}{J\Omega} & \hat{\mu}_{ai} &= \frac{c_{ai}}{m_i\Omega} & I_i &= m_i R_{io}^2 \\ b_i &= \frac{I_i}{J} & \Gamma_o &= \frac{T_o}{J\Omega^2} & \hat{\Gamma}_\theta &= \frac{\hat{T}_\theta}{J\Omega^2} \end{aligned} \right\} \quad (2.9)$$

and,

$$x_i(s_i) = \frac{R_i^2(s_i)}{R_{io}^2} \quad \text{and} \quad g_i(s_i) = \sqrt{x_i(s_i) - \frac{1}{4} \left(\frac{dx_i}{ds_i}(s_i) \right)^2}.$$

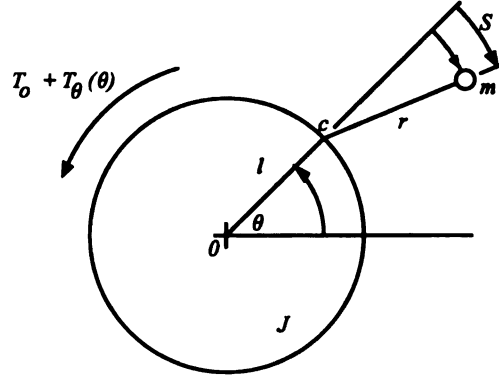


Figure 2.2. Single absorber, circular path CPVA defining the parameters used in Equation 2.10.

2.4 Absorber Tuning and System Resonance

In order to gain an appreciation for the subsequent work, it is convenient to look into the linearized equations of motion. From these, it is possible to determine the absorber tuning, \tilde{n} , and the applied torque order that will result in resonant conditions of the complete system. Using the model shown in Figure 2.2, the linearized equations of motion are:

$$\left. \begin{aligned} (J + m_i(l + r)^2)\ddot{\theta} + c_o\dot{\theta} + m_i(rl + r^2)\ddot{\phi} &= T_o + \hat{T}_\theta \sin n\theta \\ (l + r)\ddot{\theta} + \ddot{S}_i + \frac{c_{ai}}{m_i}\dot{S}_i + \left(\frac{l}{r}\dot{\theta}^2\right)S_i &= 0. \end{aligned} \right\} \quad (2.10)$$

2.4.1 Absorber Tuning

Each of the N absorbers has a natural frequency, ω_n , that can be determined from the linearized equations of motion, Equation 2.10, by assuming the angular speed of the rotor is constant, i.e. $\dot{\theta} = \Omega$. Under this condition, $\omega_n = \Omega\tilde{n}$ where

$$\tilde{n} = \sqrt{\frac{l}{r}}. \quad (2.11)$$

The \tilde{n} represents a fixed quantity determined by the geometry of the absorber system shown in Figure 2.2. It can be shown that if $\tilde{n} = n$ and the absorber damping is zero (or small), the resulting angular acceleration of the rotor, $\ddot{\theta}$, will be zero (or small) even if $\hat{T}_\theta \neq 0$. Specific values for l and r will be presented in the next chapter.

2.4.2 System Resonance

The rotor/absorber system of Figure 2.2 has two natural frequencies, which can be easily found from Equation 2.10. In future analysis it will be convenient to know the order at which resonance occurs. The first natural frequency occurs at 0, which corresponds to a rigid body mode. The second natural frequency is

$$\omega_2 = \Omega \sqrt{\frac{l}{r} \left(1 + \frac{1}{J} \sum_{i=1}^N m_i (r+l)^2 \right)} = \Omega n_2. \quad (2.12)$$

The resonant order is defined from the above equation as

$$n_2 = \sqrt{\frac{l}{r} \left(1 + \frac{1}{J} \sum_{i=1}^N m_i (r+l)^2 \right)}. \quad (2.13)$$

Using the definition of b_i (Equation 2.9), Equation 2.13 becomes

$$n_2 = \sqrt{\frac{l}{r} \left(1 + \sum_{i=1}^N b_i \right)} = \tilde{n} \sqrt{1 + \sum_{i=1}^N b_i}, \quad (2.14)$$

which shows that the resonance is close to the absorber tuning, \tilde{n} , since typically $b_i \ll 1$.

2.5 General Path Function

In Section 2.2, $X_i(S_i)$ was introduced such that any variety of absorber paths could be studied by simply specifying this function.

In this dissertation the CG will follow an epicycloidal path tuned to order \tilde{n} . A detailed description of what is meant by an epicycloidal path is deferred until Section 2.11. To continue with the current analysis we will follow the work of Chao [2] who has shown that an epicycloidal path can be described by

$$x_i(s_i) = 1 - \tilde{n}^2 s_i^2. \quad (2.15)$$

With the path function for an epicycloid specified, $g_i(s_i)$ and $\frac{dg_i}{ds_i}(s_i)$ become

$$g_i(s_i) = \sqrt{1 - (\tilde{n}^2 + \tilde{n}^4)s_i^2} \quad \text{and} \quad \frac{dg_i}{ds_i}(s_i) = \frac{-(\tilde{n}^2 + \tilde{n}^4)s_i}{\sqrt{1 - (\tilde{n}^2 + \tilde{n}^4)s_i^2}}. \quad (2.16)$$

The absorber motion is restricted by $g_i(s_i)$ in the sense that it must be kept real during absorber motion [2]. The physical reason for this will be presented in Section 3.1.4. However, experimentally there are far greater restrictions imposed on the absorber motion. These will be discussed in Section 4.1.

2.6 Scaling

In the sections to follow the method of averaging will be employed to develop approximate steady state solutions for the angular acceleration of the rotor and absorber motion. Therefore, there is a need to define a small parameter that can be used to correctly scale the terms in the equations of motion. Recall that the ratio of the inertia of an absorber to the inertia of the rotor is defined as b_i . This is physically

likely to be small, therefore we will define the needed parameter, ϵ , to be

$$\epsilon \equiv \sum_{i=1}^N b_i = \frac{1}{J} \sum_{i=1}^N m_i R_{io}^2. \quad (2.17)$$

This is the inertia ratio of all unlocked absorbers to the rotor inertia. Using this definition other system parameters can now be scaled such that the equations of motion will be in the appropriate form for the method of averaging. The following system parameters that appear in Equations 2.7 and 2.8 are therefore redefined to recognize that they are small quantities. The necessary system parameters scaled by ϵ become,

$$\hat{\mu}_{ai} = \epsilon \tilde{\mu}_{ai}, \quad \hat{\mu}_o = \epsilon \tilde{\mu}_o, \quad \Gamma_o = \epsilon \tilde{\Gamma}_o, \quad \text{and} \quad \hat{\Gamma}_\theta = \epsilon \tilde{\Gamma}_\theta. \quad (2.18)$$

These $O(\epsilon)$ terms can now be substituted back into Equations 2.7 and 2.8. For more details about the scaling see Chao [2].

2.7 Approximate Equations of Motion

The following results are a brief summary from the work of Chao [2]. Chao has shown that the first order approximation of the rotor angular acceleration and the absorber equations of motion are,

$$vv'(\theta) = -\epsilon \left\{ \frac{1}{N} \sum_{j=1}^N \left(-2\tilde{n}^2 s_j s'_j - \tilde{n}^2 g_i(s_j) s_j + \frac{dg_j}{ds_j}(s_j) s_j'^2 \right) - \tilde{\Gamma}_\theta \sin n\theta \right\} + O(\epsilon^2) \quad (2.19)$$

and

$$s_i'' + \tilde{n}^2 s_i = \epsilon f + O(\epsilon^2) \quad (2.20)$$

respectively, with

$$f = -\tilde{\mu}_a s_i + (s'_i + g_i(s_i)) \left[\frac{1}{N} \sum_{j=1}^N (-2\tilde{n}^2 s_j s'_j - \tilde{n}^2 g_j(s_j) s_j + \frac{dg_j}{ds_j}(s_j) s_j'^2) - \tilde{\Gamma}_\theta \sin n\theta \right].$$

Now that Equation 2.20 is uncoupled from the rotor equation it is possible to solve for the absorber motion, s . This is then substituted back into Equation 2.19 which allows for the angular acceleration of the rotor to be obtained.

2.8 Mistuning

It is of interest to examine the effects of mistuning between \tilde{n} and n . Mathematically this is accomplished by introducing a mistuning parameter σ , which will be defined as

$$\tilde{n} = n(1 + \epsilon\sigma). \quad (2.21)$$

Substituting the mistuning into Equation 2.20 yields a new equation for the absorber motion:

$$s''_i + n^2 s_i = \epsilon(f - 2\sigma n^2 s_i) + O(\epsilon^2). \quad (2.22)$$

2.9 Method of Averaging

The method of averaging will now be employed to find the first order approximate solutions to Equation 2.22. Following the usual procedure, (see Chao [2] for details), a transformation is made to polar coordinates

$$s_i = a_i \cos(\phi_i - n\theta) \quad \text{and} \quad s'_i = na_i \sin(\phi_i - n\theta). \quad (2.23)$$

Next the above transformation is substituted into Equation 2.22 and integrated over one period. The averaged values of a_i and ϕ_i are now expressed as r_i and φ_i , respectively. The result from this operation may be found in Chao [2](Equation 3.12).

These averaged first order equations will be further simplified by assuming that each absorber is identical ($m_i = m, c_{ai} = c_a$) and that the absorbers undergo unison motion,

$$r_i = r \quad \text{and} \quad \varphi_i = \varphi \quad \text{for} \quad 1 \leq i \leq N. \quad (2.24)$$

With Equation 2.24, the resulting averaged equations are

$$r' = \epsilon \left\{ -\frac{1}{2}\tilde{\mu}_a r + \frac{\tilde{\Gamma}_\theta}{n} \cos(\varphi) F_1(r) \right\} \quad (2.25)$$

and

$$\varphi' = \epsilon \left\{ -\frac{\tilde{\Gamma}_\theta}{nr} \sin(\varphi) F_2(r) + \left(\frac{1}{4}n^5 r^2 - \frac{n}{2} \right) - n\sigma \right\} \quad (2.26)$$

where,

$$\left. \begin{aligned} F_1(r) &= \frac{1}{2\pi} \int_0^{2\pi} \sin^2 x [1 - (\tilde{n}^2 + \tilde{n}^4)r^2 \cos^2 x]^{\frac{1}{2}} dx \\ F_2(r) &= \frac{1}{2\pi} \int_0^{2\pi} \cos^2 x [1 - (\tilde{n}^2 + \tilde{n}^4)r^2 \cos^2 x]^{\frac{1}{2}} dx \end{aligned} \right\}. \quad (2.27)$$

With all absorbers identical, the following quantities have been defined such that they inherently account for the number of absorbers present:

$$c_{ao} = Nc_a \quad m_o = Nm_i \quad I_o = NI_i. \quad (2.28)$$

Where J is equal to the inertia of the rotor plus the inertias of all absorbers locked at their vertices and I_o is the total inertia of all unlocked absorbers, $I_o = m_o R_o^2$.

Similarly the damping coefficient, $\hat{\mu}_{ai}$, has become

$$\hat{\mu}_a = \frac{Nc_a}{Nm\Omega} = \frac{c_{ao}}{m_o\Omega}. \quad (2.29)$$

Further insight into the damping will be given in Section 3.3. In particular, experimentally determined values for $\hat{\mu}_a$ will be determined from measured damping ratios, ζ .

2.9.1 Approximate Steady State Solutions

The steady state values of r and φ are now determined by setting $r' = \varphi' = 0$ in Equations 2.25 and 2.26, which results in

$$\begin{aligned}\bar{\Gamma}_\theta \cos \varphi &= \frac{\tilde{\mu}_a \tilde{n} r}{2F_1(r)} \\ \bar{\Gamma}_\theta \sin \varphi &= \left(\left(\frac{1}{4} \tilde{n}^5 r^2 - \frac{\tilde{n}}{2} \right) - \sigma \tilde{n} \right) \frac{\tilde{n} r}{F_2(r)},\end{aligned}\quad (2.30)$$

where $n \simeq \tilde{n}$ to order ϵ has been employed. Squaring and adding both sides results in an expression for absorber motion versus applied torque as

$$\bar{\Gamma}_\theta = \sqrt{\left(\frac{\tilde{\mu}_a \tilde{n} r}{2F_1(r)} \right)^2 + \left(\left(\frac{1}{4} \tilde{n}^5 r^2 - \frac{\tilde{n}}{2} \right) - \sigma \tilde{n} \right) \frac{\tilde{n} r}{F_2(r)} }^2 \quad (2.31)$$

2.10 General Response for Various Path Types

In Chapter 1 the short comings of circular and cycloidal paths were discussed. In both cases the effects of nonlinearities could cause mistuning of the absorber at large absorber amplitudes. This mistuning introduces the possibility of jump bifurcations to large amplitude absorber motion. Since both the circular and cycloidal paths cause amplitude dependence, the circular path will be chosen as the representative case. Its influence on the absorber motion will be compared and contrasted to the equivalent system moving along an epicycloidal path. Approximate steady solutions will be obtained from Equations 2.30 and 2.31 (for epicycloid case) and the associated equations for the circular case (see Equations 2.23 and 2.24 in Alsuwaiyan [3]).

2.10.1 Effects of Varying Torque Order on Angular Acceleration

When the order of the applied torque is increased, the magnitude of the angular acceleration begins to decrease as it approaches the tuning of the absorbers, see Figure 2.3. The magnitude of the angular acceleration will eventually reach a minimum value when forced near \tilde{n} , which corresponds to the small amplitude absorber tuning. Once the applied torque order is increased past \tilde{n} and begins to approach the second natural frequency of the system, n_2 , (see Equation 2.12), the influence of the path type on angular acceleration becomes distinguishable. The circular path type exhibits jump bifurcations to large amplitude values in both angular acceleration and absorber motion. However, the epicycloid path does not exhibit any such jump bifurcations. It is also interestingly to note that from Equation 2.14 that n_2 becomes very close to \tilde{n} as ϵ decreases. This results in a very sudden rise in the rotor's angular acceleration as $n > \tilde{n}$.

Although not shown here the cycloidal path differs from the circular path near resonance. Near resonance the circular case bends to the left, the opposite is encountered with the cycloidal path.

2.10.2 Effects of Absorber Amplitude on Tuning Order

In the circular case, as the absorber amplitude grows the tuning order shifts to the left. To demonstrate this Figure 2.3 is replotted to an enlarged scale in Figure 2.4. They clearly show the dependence of the tuning order versus the absorber amplitude at various increasing levels of applied torque. The epicycloidal path does not share this amplitude dependence. As seen from the figure, the minimum point occurs at the same order for each level of applied torque.

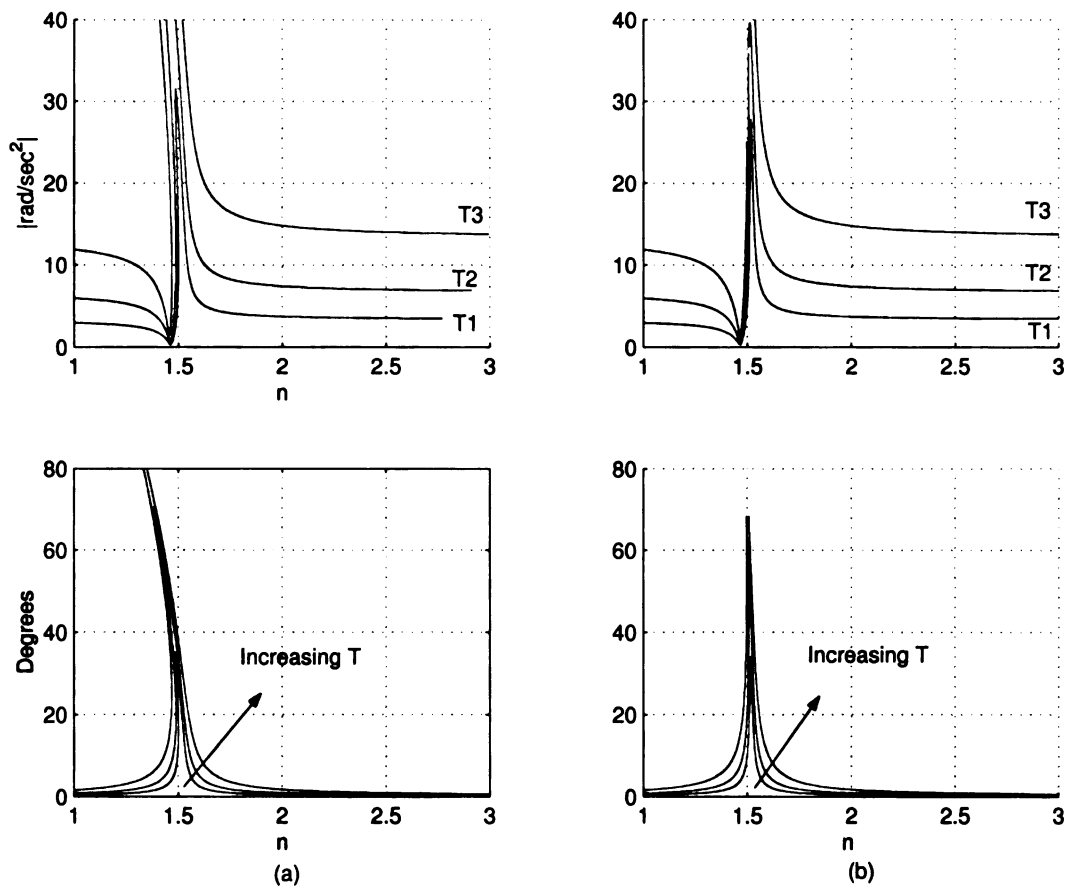


Figure 2.3. Effects of varying torque order on $|\ddot{\theta}|$ and absorber motion for (a) circular path absorbers (b) epicycloidal path absorbers, where $T_2=2T_1$; $T_3=2T_2$.

2.11 The Epicycloid Path

The epicycloid path is the path traced out by a point on the circumference of a circle of radius b rolling without slipping on the outside of a base circle of radius a . This point is labelled as m_i in Figure 2.5 since it physically represent the CG of the i -th absorber. This path will be referred to as the involute of the epicycloid. Likewise, the evolute of the epicycloid is a scaled version of the involute, scaled by a factor of $\frac{a}{a+2b}$, and shifted such that the minimum of the evolute corresponds to the maximum of the involute, (as shown in Figure 2.5). The evolute physically corresponds to the

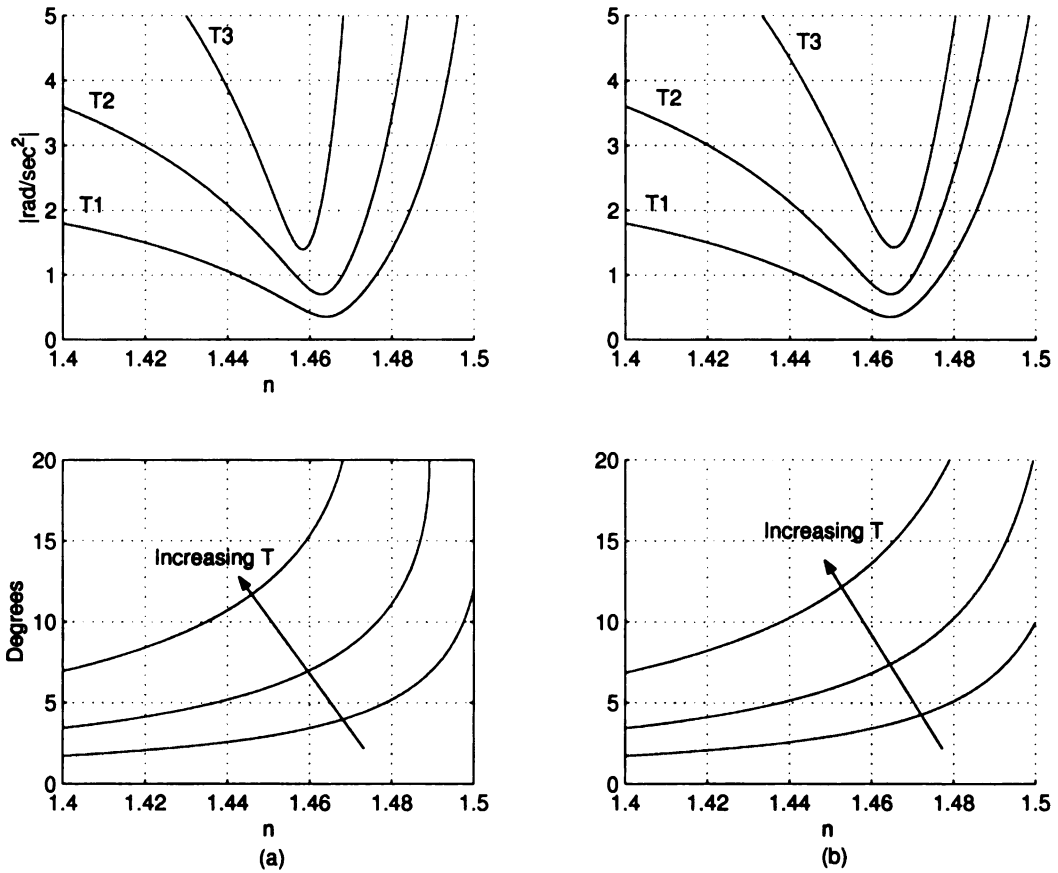


Figure 2.4. Effects of torque amplitude on absorber tuning and absorber amplitude for (a) circular path absorbers (b) epicycloidal path absorbers, where $T_2=2T_1$; $T_3=2T_2$.

cheeks used in the experimental application of the epicycloid CPVA.

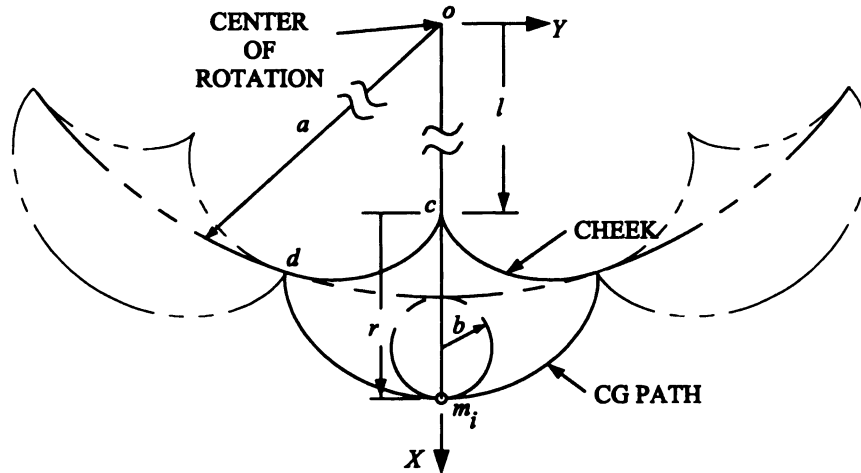


Figure 2.5. Epicycloid Path.

Physically the CG of the absorber is constrained to follow the prescribed path by using a flexible and inextensible material connecting the absorber to the base of the cheeks at point c . Assuming that the flexible material is always under tension, as m_i moves along the CG path the flexible material begins to follow the contour of the cheeks. This is shown in Figure 2.6. Experimentally the evolute of the epicycloid is used to constrain the CG of the absorber to follow the path defined by Equations 2.32.

2.11.1 The Involute

The involute of the epicycloid is easily found for a point m_i , as shown in Figure 2.5. With the point m_i oriented as shown, the following parametric equations define the

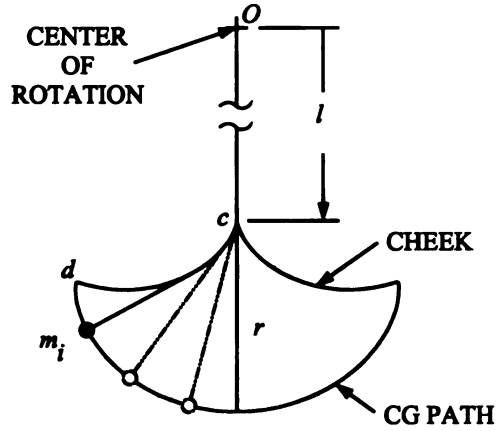


Figure 2.6. Constrained path of CG following contour of the cheek with inextensible flexible bands.

path that the point will move through,

$$\begin{aligned} x_{inv}(\beta) &= (a + b) \cos \beta + b \cos \frac{(a+b)}{b} \beta \\ y_{inv}(\beta) &= (a + b) \sin \beta + b \sin \frac{(a+b)}{b} \beta \end{aligned} \quad (2.32)$$

where β is a dummy variable used to construct the geometry of the involute.

Design wise, the desired value of the absorber tuning, \tilde{n} , and R_o will be set. Using the geometry described in Figure 2.5 and recalling Equation 2.11, one can easily find the relationships

$$\begin{aligned} a &= \frac{R_o \tilde{n}}{\sqrt{\tilde{n}^2 + 1}} \\ b &= \frac{R_o}{2} \left(1 - \frac{\tilde{n}}{\sqrt{\tilde{n}^2 + 1}} \right) \end{aligned} \quad (2.33)$$

where we have used the geometric relationship

$$l = \left(\frac{a}{a + 2b} \right) a. \quad (2.34)$$

Hence we now can solve for a and b , given \tilde{n} and R_o .

2.11.2 The Evolute

Recognizing that the evolute (the cheeks) are simply scaled versions of the involute we can immediately obtain their cartesian coordinates as

$$\begin{aligned}x_{evo}(\beta) &= \frac{a}{a+2b} \left((a+b) \cos \beta - b \cos \frac{(a+b)}{b} \beta \right) \\y_{evo}(\beta) &= \frac{a}{a+2b} \left((a+b) \sin \beta - b \sin \frac{(a+b)}{b} \beta \right) .\end{aligned}$$

Noting that the signs have been changed to put point c at its minimum point, in accordance with geometric relationships mentioned previously.

CHAPTER 3

Experimental Setup and Physical Parameters

The experimental setup will be described in this chapter along with a discussion on how the dynamic data is extracted and processed.

Details of the empirically measured system parameters will also be presented, i.e., the absorber tuning (\tilde{n}), absorber damping ratio (ζ), inertia of the rotor and all locked absorbers (J_{Locked}), and the mass of each absorber m_i will all directly be measured for the system. Knowing these numerical values allows for the following parameters to be calculated: absorber inertia (I_o), absorber damping ($\hat{\mu}_{ao}$), inertia ratio (ϵ), rotor inertia (J), and the resonant order (n_2).

3.1 Experimental Setup

A schematic of the experimental setup is shown in Figure 3.1 indicating the major components and the path of the signals used to control and measure the experiment.

torque.

3. To measure the instantaneous speed, $\dot{\theta}(t)$, of the rotor.

The signal $\dot{\theta}(t)$ mentioned in item three is obtained by passing the TTL pulses from the motor encoder through a frequency to voltage converter (F2V). The output for this device is an analog voltage that is proportional to $\dot{\theta}(t)$. This signal is routed to the Labview Data Logger, real-time FFT analyzer, and a 1 Hz low-pass filter.

The purpose of the low-pass filter is to extract the DC component from the $\dot{\theta}(t)$ signal, i.e. the mean speed, Ω . Ideally, this should be constant but in practice it was found to slowly drift, on a time scale of approximately 5-10 seconds. Therefore, a secondary control system was established to ensure that this slow drift was negated. This is marked as a dashed line in Figure 3.1. The net result is a very slowly varying voltage that is proportional to the T_o component required to maintain the constant mean rotor speed, Ω . In all of the experiments to be reported in Chapter 4, this mean speed was fixed at 300 rpm.

Returning to item two, the alternating component of the torque is combined with T_o in the adder shown in Figure 3.1. It is important to note that a sinusoidal function of angular position is required (i.e., $\hat{T}_\theta \sin(n\theta)$ and not $\hat{T}_\theta \sin(n\Omega t)$). This is accomplished by generating, in a Labview program, a sine wave that is based on the TTL signal from the motor encoder. Each pulse from the encoder represents an angular change of $\frac{2\pi}{1000}$ rad. Hence, for the i -th pulse in the sequence, we need the Labview program to generate an analog output proportional to $\hat{T}_\theta \sin(n\frac{i2\pi}{1000})$. This is accomplished in real time and works for real values of n from 1 to 10.

3.1.2 Absorber Measuring Devices

The absorber position is measured using encoders (supplied by USDigital S5D-360-LB). Differential optical encoders were chosen to eliminate noise that is generated

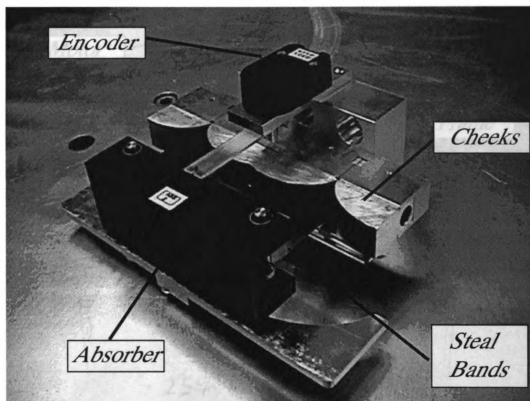


Figure 3.2. Close up of Absorber highlighting various parts.

along the signal path. The encoder shaft is centered at point c (see Figure 2.5) and uses a lightweight arm to measure the angular position of the CG of the absorber (Figure 3.2). The wiring of the encoders is passed down the shaft and connected to a 20 channel slip-ring. From the slip-ring the signals from the encoders go into a differential receiver (USDigital EA-R8), which converts them to single-ended TTL outputs. A specialized board (MicroStar MSXB 023) and a Labview program converts these quadrature signals into degrees.

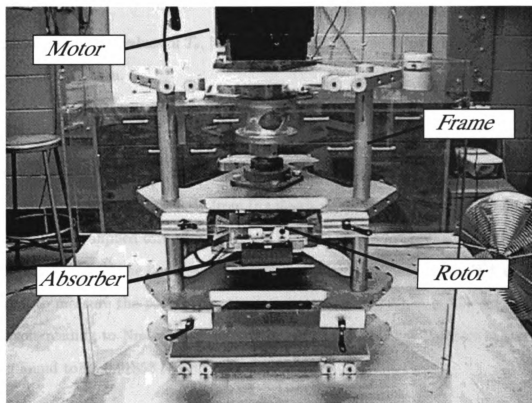


Figure 3.3. Physical experimental setup.

3.1.3 Absorber and Rotor

The frame, rotor, and absorber assembly are labelled in Figure 3.3. The rotor consists of: the main shaft that is connected to the motor through a coupler; a steel flywheel that can accommodate up to four absorber; and the base parts of the absorber assembly that are attached to the flywheel. The absorbers are attached to the absorber assembly in a bifilar fashion. Figure 3.2 shows is closeup of the actual implementation of the epicycloidal path CPVA. The absorber is attached to the flywheel through 0.002" blue tempered spring steal bands. Visible in this figure is the encoder used to measure the angle of the absorber and the cheeks that are located either side of the spring steal bands that constrain the absorber's CG to follow an epicycloid.

3.1.4 Experimentally Obtained Values

Experimentally, the values of \hat{T}_θ , $|\ddot{\theta}|$, and $|S|$ need to be measured. Each of these will be discussed in turn.

Obtaining \hat{T}_θ

The fluctuating torque, \hat{T}_θ , is obtained by measuring a voltage that is proportional to the applied torque taken directly from the motor controller. This voltage is made up of the constant applied torque, T_o , and the fluctuating applied torque, \hat{T}_θ . Of interest is the magnitude of the fluctuating applied torque at the order, n . An FFT analyzer is used to measure the peak corresponding to the applied order, n . To convert this millivolt reading to Nm it must be multiplied by a calibration constant. That has been found to be 0.01853 Nm/mV.

Obtaining $|\ddot{\theta}|$

The angular rotor acceleration, $|\ddot{\theta}|$, is not measured directly. Instead, the $\dot{\theta}(t)$ signal that leaves the F2V is feed into the FFT analyzer. The peak that corresponds to the applied order, n , is recorded and then multiplied by $n\Omega$ to convert it into an acceleration.

Obtaining S

The equation of motion of the absorber is written in terms of the arc length, S . However, experimentally this length is difficult to measure and so the angle the CG moves through is measured using optical encoders. Now S needs to be expressed in terms of the measured angle, ϕ .

Using the parametric equations for the involute (Equation 2.32), it is possible to

determine the arc length, S , by using the relationship

$$S = \int_0^\beta \sqrt{\left(\frac{dx_{inv}}{d\beta}(\beta)\right)^2 + \left(\frac{dy_{inv}}{d\beta}(\beta)\right)^2} d\beta,$$

which simplifies to,

$$S = \frac{4b(a+b)}{a} \sin\left(\frac{a\beta}{2b}\right). \quad (3.1)$$

Now, an expression relating the measured angle ϕ to the dummy variable, β , will be obtained. To do this, the origin must be moved to coincide with the actual location that ϕ is measured from, i.e., from point O to point c (see Figure 2.5). The angle ϕ (see Figure 3.5), is then described by

$$\phi = \tan^{-1}\left(\frac{y_{inv}(\beta)}{x_{inv}(\beta) - l}\right). \quad (3.2)$$

Using Mathematica and the physical parameters obtained in this chapter, it is possible to show numerically the relationship between ϕ and S (see Figure 3.4). Surprisingly, the relationship seems to be linear, resulting in

$$\phi = \frac{S}{r}. \quad (3.3)$$

It is interestingly to note that the relationship found here is the same as the arc length of a circle of radius r whose center is at point c . It is likely that this relationship could be proved. To better visualize this, Figure 3.5 compares the circular path to that of the epicycloid path. Both paths shown are tuned to the same order.

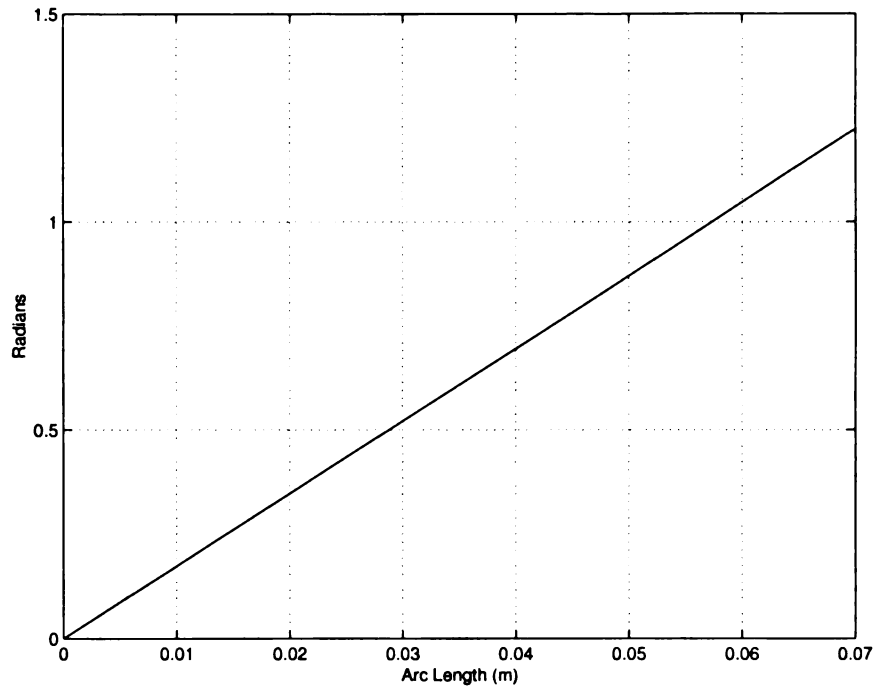


Figure 3.4. Relationship between arc length S and absorber angle, ϕ , measured from point c in Figure 2.6.

3.2 Absorber Lengths

The quantity r can easily be measured from the experimental apparatus. It is simply the length of the flexible steal bands and is found to be $r = 0.0576\text{m}$. Rather than experimentally finding the exact position of the absorber's CG, the distance l is found indirectly from the measured absorber tuning, $\tilde{n} = 1.465$ (this value will be reported in Section 4.3). Hence recognizing that $\tilde{n}^2 = \frac{l}{r}$ we find $l = 0.1236\text{m}$. If required, R_o can be calculated from the relationship $R_o = l + r$.

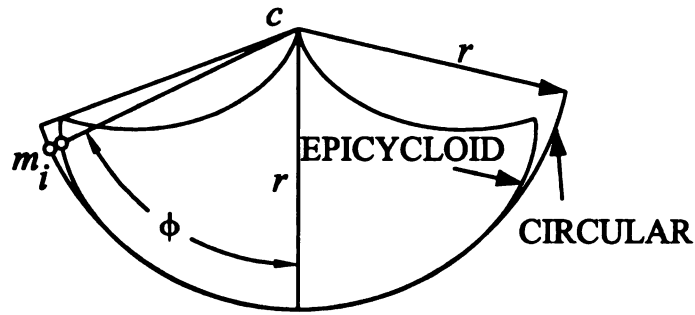


Figure 3.5. Epicycloidal path compared to a circular path of radius r , both paths are tuned to same order \tilde{n} .

3.3 Damping

The damping mechanisms in the system are likely to be quite complicated. However in this investigation it is assumed to be viscous throughout. The damping on the rotor was discussed in the previous chapter and serves only to balance the constant applied torque, T_o , thus fixing the mean speed, Ω . The absorber damping will now be discussed.

3.3.1 Absorber Damping Ratio

The following derivation of the damping ratio, ζ , is conducted on only one absorber. The damping ratio will be found experimentally by running the rotor at a constant mean speed and applying sufficient fluctuating torque, \hat{T}_θ , to cause the absorber to exhibit large amplitude motion. The fluctuating torque will then be immediately cut off to allow the absorber to experience free vibration. Shown in Figure 3.6 is the resulting angular displacement of the absorber from this test. Next the log decrement method is utilized yielding a damping ratio of $\zeta=.00344$.

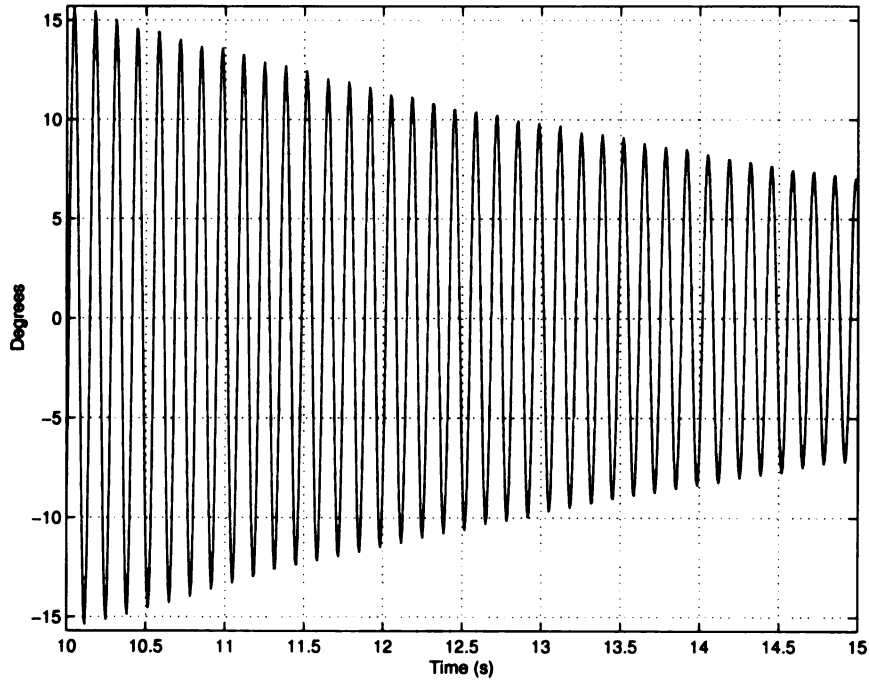


Figure 3.6. Angular displacement of an absorber showing the amplitude decay as a function of time.

3.3.2 Non-dimensional Damping Factor

Assuming a constant rotor speed (i.e. $\ddot{\theta} = 0$), Equation 2.3 reduces to

$$m_o \left[\ddot{S} - \frac{1}{2} \frac{dX}{dS}(S) \Omega^2 \right] = -c_{ao} \dot{S}. \quad (3.4)$$

Using Equation 2.15, noting that

$$\frac{dX}{dS}(S) = -2\bar{n}^2 S$$

and using Equation 3.3, e.g. $S = r\phi$, and some dimensionless substitutions introduced in Chapter 2.3, Equation 3.4 reduces to the following form,

$$\ddot{\phi} + \frac{c_{ao}}{m_o} \dot{\phi} + (\tilde{n}\Omega)^2 \phi = 0. \quad (3.5)$$

Comparing this to the desired form of a viscously damped linear oscillator

$$\ddot{\phi} + 2\zeta\Omega\tilde{n}\dot{\phi} + (\Omega\tilde{n})^2 \phi = 0, \quad (3.6)$$

we have

$$\frac{c_{ao}}{m_o} = 2\zeta\Omega\tilde{n} \quad (3.7)$$

and so, from Equation 2.29

$$\hat{\mu}_a = 2\zeta\tilde{n}. \quad (3.8)$$

3.4 Absorber and Rotor Inertias

Determining the respective inertias will serve to fix the small parameter, ϵ . The total inertia, J_{Locked} , will first be determined by locking all absorbers and recording the magnitude of the angular acceleration at various levels of increasing \hat{T}_θ for an arbitrary applied torque order. Then the rotor inertia, J , will be found by subtracting I_o from J_{Locked} .

3.4.1 Total Inertia

Figure 3.7 shows the experimental results of a test completed with all absorber locked, running at $n=1.40$. Since $Torque = Inertia * Angular Accerleration$, determining the slope of this graph will allow one to determine the total inertia. The total inertia for the system is found to be $J_{Locked}=0.0811 \text{ kgm}^2$.

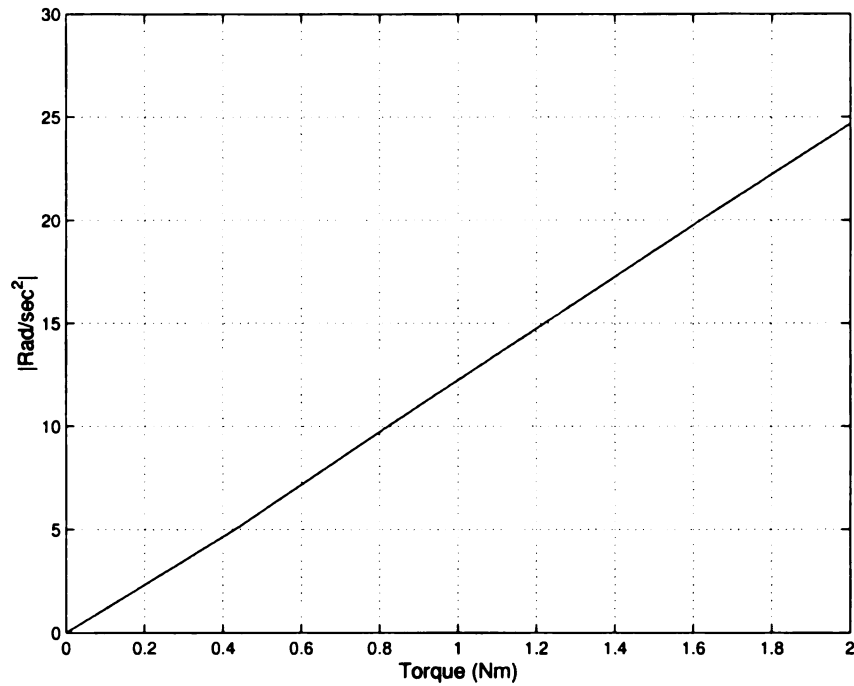


Figure 3.7. $|\ddot{\theta}|$ versus \hat{T}_θ with all absorbers locked, $n=1.40$.

3.4.2 Absorber Inertia

The absorber inertia is not obtained directly. Instead the absorber's mass is measured and then multiplied by R_o^2 to obtain I_o . Recalling that I_o describes the inertia of all unlocked absorbers, and that the measured mass of one absorber is 0.173 kg, we have

$$I_o = m_o(R_o)^2 = N * 0.173(R_o)^2.$$

The inertia of the rotor, J , is then obtained by,

$$J = J_{Locked} - I_o.$$

Physical values for various numbers of unlocked absorbers are shown in Table 3.1. Included in this table are the inertias of the absorbers, rotor, and ϵ .

Table 3.1. Various inertias and ϵ values for different N 's.

N	I_o ($kg * m^2$)	J ($kg * m^2$)	ϵ
1	.00568	.07542	.07531
2	.01136	.06974	.16290

3.5 System Resonance

The system resonance may be found in accordance with Equation 2.13. Table 3.2 shows the associated values for the resonant order, n_2 .

Table 3.2. System resonant orders at various number of unlocked absorbers.

N	n_2
1	1.519
2	1.579

3.6 Parameter Summary

A summary of the physical parameters obtained in this chapter are shown in Table 3.2.

Table 3.3. Summary of physical parameters obtained experimentally.

Parameter	Values	Description
l	.1236 m	Length O to c from Figure 2.5
r	.0576 m	Length c to m in orientation shown, Figure 2.5
R_o	.1812 m	Length O to m in orientation shown, Figure 2.5
\tilde{n}	1.465	Tuning of each absorber
ζ	.00344	Absorber damping ratio
I_o (N=1)	.00568 kg*m ²	Absorber inertia for one active absorber
I_o (N=2)	.01136 kg*m ²	Absorber inertia for two active absorbers
ϵ (N=1)	.075314	Inertia ratio for one active absorber
ϵ (N=2)	.162890	Inertia ratio for two active absorber
n_2 (N=1)	1.519	Resonant order for one active absorber
n_2 (N=2)	1.579	Resonant order for two active absorbers
J (N=1)	.07542 kg*m ²	Inertia of rotor with one active absorber
J (N=2)	.06974 kg*m ²	Inertia of rotor with two active absorbers
J_{Locked}	.0811 kg*m ²	Inertia of rotor with all absorbers locked
Ω	10π rad/s ²	Mean speed of rotor

CHAPTER 4

Experimental Results

In the following sections the results from a series of tests on one and two absorber systems will be reported. The CPVA's performance will be evaluated using two criteria. Firstly, how effective the absorbers are at minimizing the angular acceleration of the rotor and secondly, the range of torque the system can operate over.

The tests will be conducted at various levels of mistuning and torque amplitudes. Recordings of both the magnitude of the first order angular acceleration and the absorber amplitude will be reported and compared to the approximate solutions that were derived in Chapter 2.

4.1 Experimental Limitations

It was not feasible to run the experiment at orders near 1 or 2, because the Allen Bradley AC servo motor used in this experiment generated small speed fluctuations at these orders. This interfered with measuring the true magnitude of angular acceleration. Hence the absorbers were designed to be tuned to an order close to $\bar{n} = 1.50$, thus avoiding the problem orders.

There also exists a limit to the amplitude the absorber may swing through on account of the cusp point that exist along the epicycloid paths. This can be seen in

Figure 2.5 and is marked as point *d*. It corresponds to an angular displacement of approximately $\pm 70^\circ$ measured either side of point *c* in the same figure. Mathematically, this point is associated with the value of s_i where $g_i(s_i)$ of Equation 2.16 becomes imaginary.

There are further physical limitations imposed on the absorber amplitude. Snubbers fixed to the rotor prevent the absorber from travelling any greater than $\pm 40^\circ$. In addition, amplitudes greater than 25° fatigue the metal bands used to constrain the absorber to the desired path resulting in premature failure of the metal bands. Therefore, continuous operation at high absorber angles is avoided.

4.2 Percentage Mistuning

Since experiments will be conducted for one and two absorber systems it will be convenient to quantify the mistuning using a parameter that is independent of ϵ , the inertia ratio of the system. Theoretically the mistuning is introduced using σ , but this may be misleading since it is a function of ϵ . That is, for a fixed torque order, n , the value of σ for one absorber will be different than for a two absorber case. This issue can be alleviated by introducing a percent mistuning parameter, δ , such that

$$n = \left(1 - \frac{\delta}{100}\right) \tilde{n}. \quad (4.1)$$

This now makes the mistuning independent of ϵ and will make direct comparisons for both one and two absorber cases easier to make.

4.3 Experimental Absorber Tuning

In this first test the applied torque order is gradually increased to observe where the angular acceleration reaches a minimum value. Three different levels of \hat{T}_θ are used

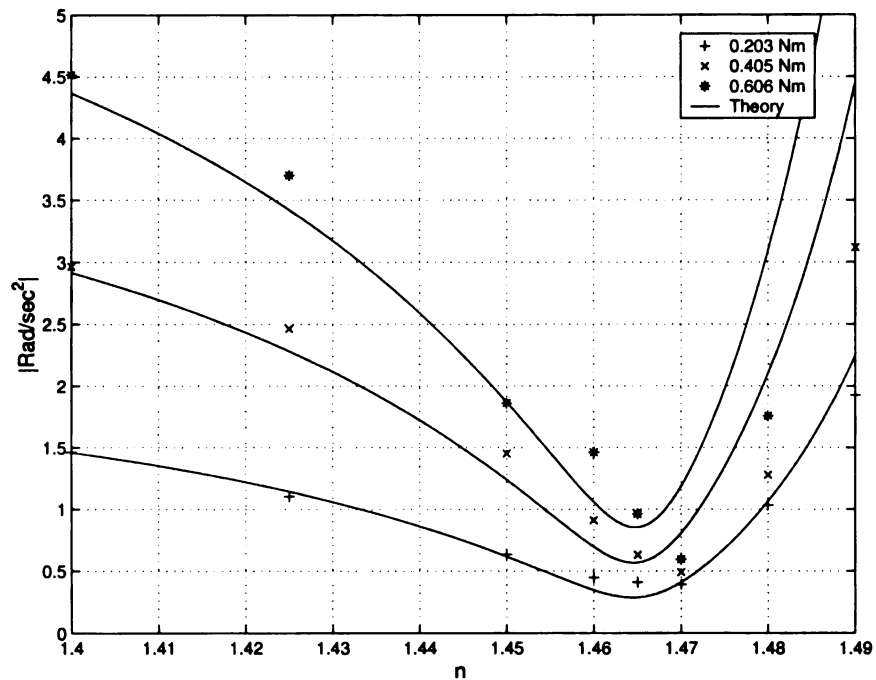


Figure 4.1. Rotor angular acceleration versus applied torque order, n , at three different \hat{T}_θ values.

to verify that the absorber tuning does not exhibit any amplitude dependence.

As can be seen from Figure 4.1 the magnitude of the angular acceleration reaches a minimum value at an order of 1.465. This did not change appreciably for the three different levels of \hat{T}_θ . It is concluded that the absorber tuning is not affected by the absorber amplitude over the range of torque tested.

Additional tests were completed on the second absorber and it too was found to have the same tuning order. Therefore, for the remainder of the study we will take $\bar{n} = 1.465$ for both absorbers.

4.4 Order Sweeps at Constant Values of \hat{T}_θ

In this section the effect that torque order has on $|\ddot{\theta}|$ and the absorber motion will be investigated. While holding the physical value of \hat{T}_θ constant, n will be increased and the corresponding values of $|\ddot{\theta}|$ and absorber motion will be recorded. The values will be compared to the theoretical predictions. Of particular interest is the response close to perfect tuning, \tilde{n} , which has been found to be 1.465 for all absorbers. The system resonance, n_2 , which is given by Equation 2.13 will also be studied. This depends on the inertia ratio, ϵ , and so depends on the number of unlocked absorbers.

4.4.1 One Operational Absorber

With one absorber unlocked, and \hat{T}_θ held constant at 0.198 Nm an order sweep was conducted and the results are shown in Figure 4.2. The experimental values for $|\ddot{\theta}|$ and absorber amplitude correlated quite well with the theoretical predictions. As the order increases and approaches an \tilde{n} of 1.465, $|\ddot{\theta}|$ gradually decreases and reaches a minimum value at perfect tuning. $|\ddot{\theta}|$ begins a sharp rise in the vicinity of the resonance, n_2 . This resonance was found experimentally to be at 1.52. This compared well with the theoretical value of $n_2=1.519$ given by Equation 2.14.

4.4.2 Two Operational Absorber

With two absorbers unlocked, and \hat{T}_θ held constant at 0.205 Nm an order sweep was conducted and the results are shown in Figure 4.3. As for the one absorber system, the theoretical predictions matched the experimental results quite well. As n is increased the absorber motion follows the unison motion assumption up to the area near perfect tuning, see Figure 4.3(b). It is observed that the unison motion assumption is not valid in the vicinity of \tilde{n} to n_2 . However, as the order increases past n_2 the absorber amplitudes again match one another and the unison motion

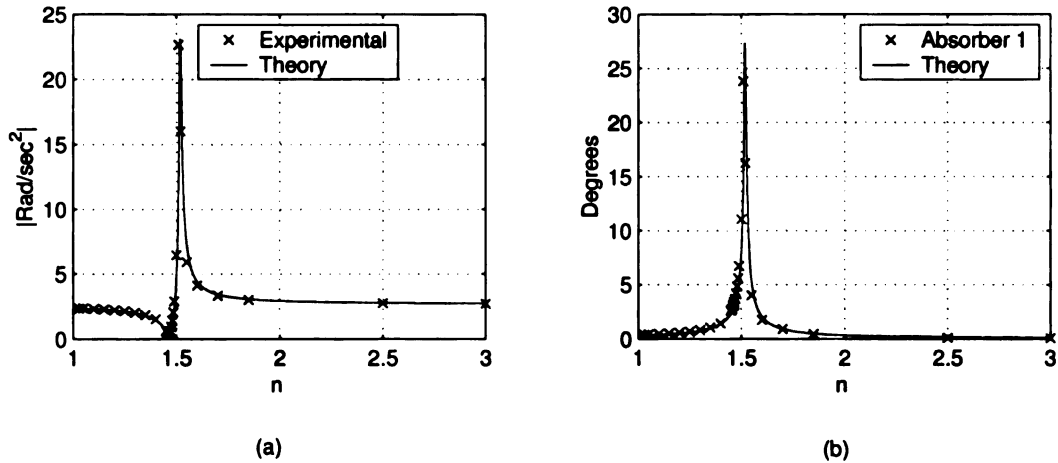


Figure 4.2. Effect of increasing order, n , at $\hat{T}_\theta = 0.198 \text{ Nm}$ and $\epsilon = 0.07531$ with one active absorbers. (a) $|\ddot{\theta}|$ of rotor, (b) absorber amplitude.

assumption becomes valid. Experimentally the resonance, n_2 , was found to be 1.58 which is in agreement with the theoretical prediction of 1.579 predicted in Section 3.5.

4.4.3 Discussion

Before discussing any of the results of Section 4.4, it should be emphasized that the type of experiment conducted here, i.e. order sweeps, are very unlikely to occur in practical applications. In almost all real-world usage, the forcing order, n , will be fixed by the type of system. For example, a single cylinder 4 stroke IC will have a dominant $n = \frac{1}{2}$ order in its torque fluctuation. However, the experimental facility has been designed to allow this order parameter to be varied. Hence, the influence of the variation between n and \tilde{n} can be easily investigated.

To this end, the order sweeps shown in Figures 4.2 and 4.3 give a very good overview of the general behavior of the complete system. The tuning order, \tilde{n} , can be clearly seen in Figures 4.2(a) and 4.3(a) (and in more detail in Figure 4.1). The value of $\tilde{n} = 1.465$ agrees closely with the theoretical predictions (see Figure 4.1) and

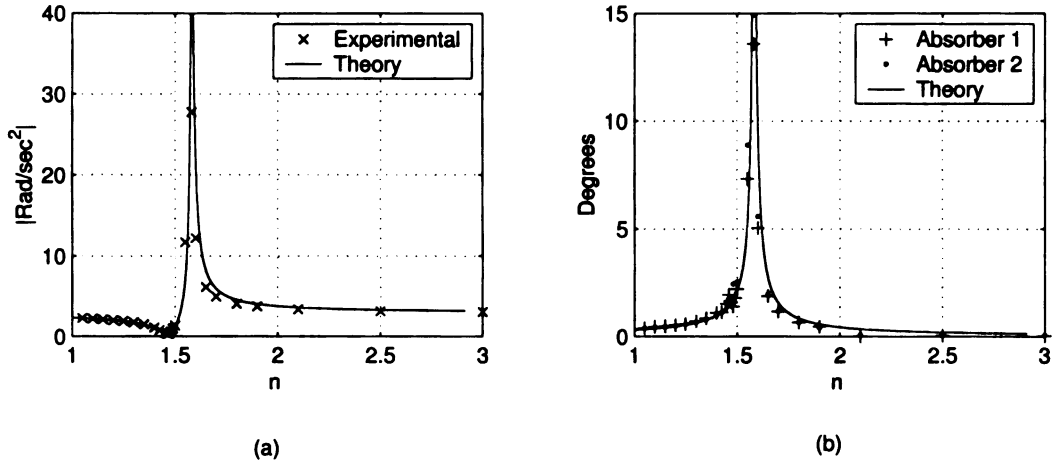


Figure 4.3. Effect of increasing order, n , at $\hat{T}_\theta = 0.205 \text{ Nm}$ and $\epsilon = 0.16290$ with two active absorbers. (a) $|\dot{\theta}|$ of rotor, (b) absorber amplitude.

the resonant peak associated with n_2 (see Equation 2.14) is measured to be 1.52 and 1.58 for the one and two absorber cases, respectively.

There are other interesting points to note from the order sweep experiments. Theoretically, as $n \ll \tilde{n}$ the absorber motions are expected to become very small, since the system is now responding well below its resonance. In this limit, as n becomes small, the absorbers act as if they were locked and so the limiting case of $|\ddot{\theta}| = \hat{T}_\theta / J_{\text{Locked}}$ should be reached. This is indeed the case and gives an independent check on the empirical value of J_{Locked} found in Section 3.4.1.

The counterpart of this is for the case of $n \gg \tilde{n}$. Now the absorbers are effectively floating in space and not responding to the applied alternating torque, i.e., the effective inertia of the system is now $J = J_{\text{Locked}} - I_o$ and thus the limiting value of $|\ddot{\theta}|$ should be $|\ddot{\theta}| = \hat{T}_\theta / J$. Again this theoretical limit is found to agree very closely to the experimental findings.

One final point worthy of comment, and discussed more fully in Section 4.5.3, is the issue of non-unison response. In the two absorber case (Figure 4.3) both absorbers

move as one over a wide range of n . However, close to $n = \tilde{n}$, an instability occurs and they no longer have the same amplitudes. With reference to Figure 4.3(b) there are ranges of n over which each absorber has a different amplitude. As stated, this will be discussed in more detail in Section 4.5.3 where torque sweep experiments are undertaken.

4.5 Torque Sweeps at Constant Values of Mistuning

In this section the effect that torque amplitude has on $|\ddot{\theta}|$ and the absorber motion will be investigated. While holding n constant, \hat{T}_θ will be increased and the corresponding values of $|\ddot{\theta}|$ and absorber motion will be recorded so that these values may be compared to the theoretical responses. Of interest here is how closely the experimental results match the theory and to study the possibility of bifurcations from the unison response.

4.5.1 One Operational Absorber

With one absorber unlocked a series of torque sweeps were performed at five different levels of mistuning. The results of these torque sweeps are shown in Figures 4.4 and 4.5. It was found experimentally that mistuning values of 5% and 3% best matched the theoretical predictions. As the mistuning approached perfect tuning, deviations from the theory became apparent.

The deviation from the theoretical predictions at and near perfect tuning may be attributed to a combination of factors. It should be recalled that both the damping ratio, ζ , and inertia ratio, ϵ , are extremely small (0.004 and 0.07531 respectively). Consequently the angular acceleration of the rotor, $|\ddot{\theta}|$, the absorber motion, S , and

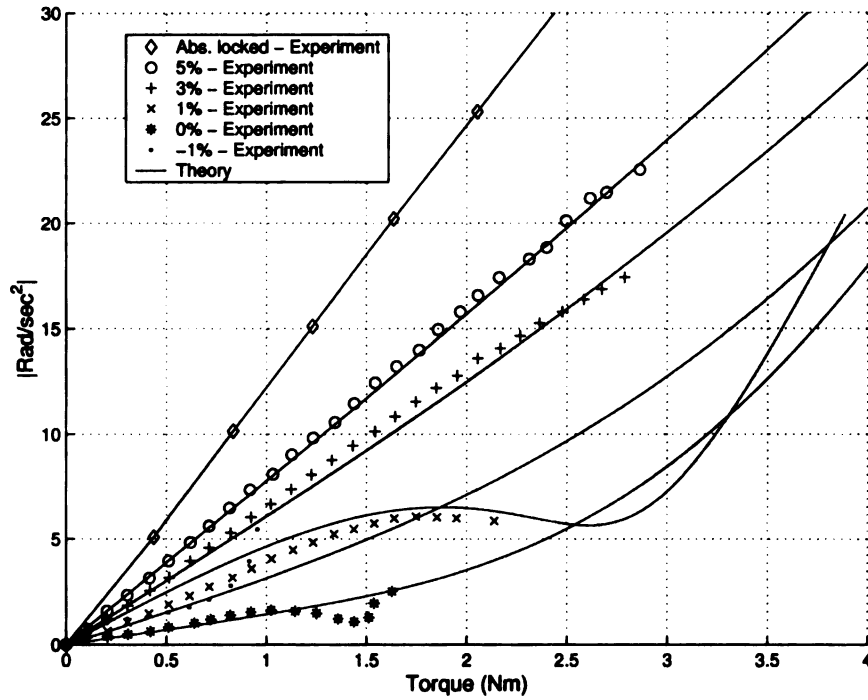


Figure 4.4. $|\ddot{\theta}|$ versus \hat{T}_θ with one absorber unlocked at various levels of mistuning.

the phase relationship between the absorber and the applied torque all become very sensitive to small changes in n , close to perfect tuning (see for example Figure 4.2). This will be discussed more fully in Section 4.5.3.

4.5.2 Two Operational Absorber

A second set of torque sweep experiments was completed for the case of two absorbers. Physically this meant that the second absorber, which was locked in place for the previous experiment, was freed. Consequently, the inertia ratio, ϵ , changes from 0.07531 to 0.16290. The test results are shown in Figures 4.6 and 4.7. Figure 4.6 is the counterpart of Figure 4.4, where the rotor's acceleration is plotted as a function of the torque, for various % of mistuning.

It should be noted that the % mistuning is independent of the number of active

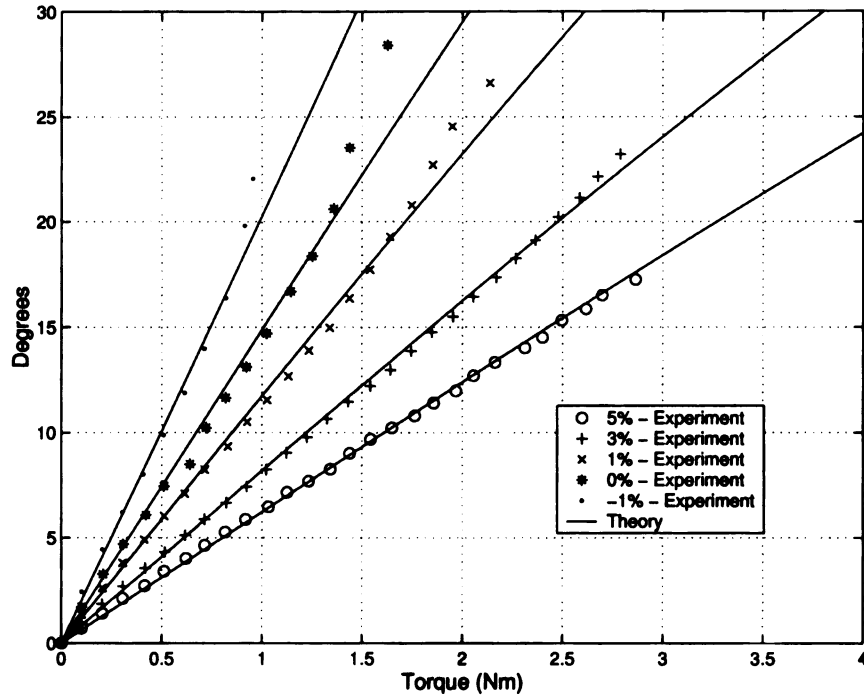


Figure 4.5. Absorber motion versus \hat{T}_θ with one absorber unlocked at various levels of mistuning.

absorbers, see Equation 4.1. That is, a mistuning of 5% corresponds to the same n of 1.392, regardless of the number of absorbers active. Hence, the figures from Section 4.5.1 can be compared directly with those in this section.

4.5.3 Discussion

One Operational Absorber

Comparing Figure 4.4 with 4.5 one may make the following observations for one unlocked absorber. Higher levels of positive mistuning (i.e. $n < \tilde{n}$) allow one to operate over a larger range of torque. However the effectiveness at reducing $|\ddot{\theta}|$ becomes worse the further one moves from $n = \tilde{n}$. At 0% mistuning the effectiveness at minimizing $|\ddot{\theta}|$ is the greatest, but the associated absorber amplitude is relatively large. The worst

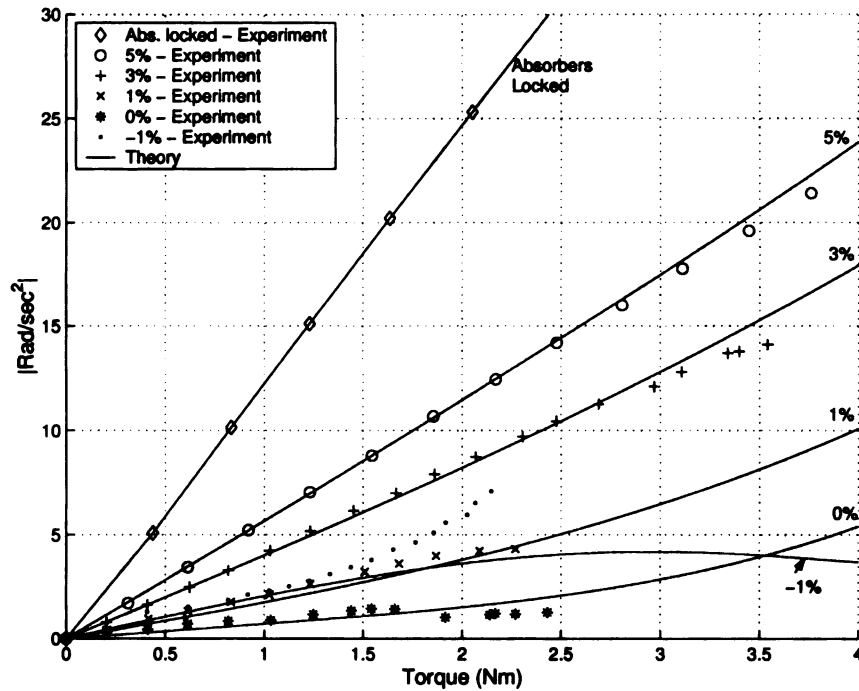


Figure 4.6. $|\ddot{\theta}|$ versus \hat{T}_θ with two absorbers unlocked at various levels of mistuning.

overall performance occurs at -1% mistuning. This is a consequence of the resonant order, n_2 , being very close to the absorber tuning, \tilde{n} . With reference to Figure 4.2, -1% mistuning ($n=1.48$), is located just to the right of perfect tuning and very close to n_2 . Hence, small changes in n have a large effect on the response.

The most likely reason for the discrepancy between theory and experimental results from the influence of the phase, ϕ , as defined in Equation 2.23. The value of ϕ is critical to the evaluation of $|\ddot{\theta}|$. The phase is very sensitive to the absorber damping in the region of n_2 and it is also likely to be affected by slow drifts in Ω . As a result, one cannot expect high correlation between theory and experimental results for $n \simeq n_2$.

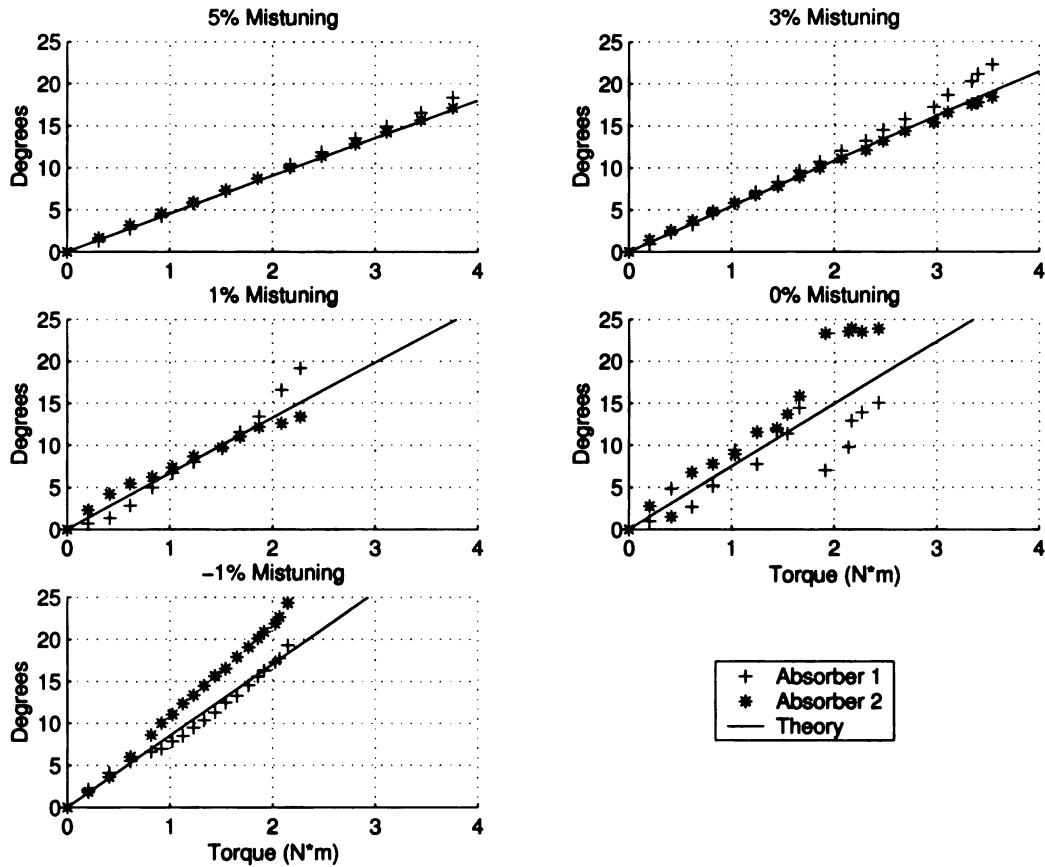


Figure 4.7. Absorber amplitudes versus \hat{T}_θ for various levels of mistuning, two absorbers unlocked.

Two Operational Absorber

The experimental results support the general theoretical trends. Since there are now two absorbers active, there is twice the inertia available to absorb $|\ddot{\theta}|$. Hence, the absorber amplitudes are smaller than in the one absorber case. Consequently higher levels of applied torque can be accommodated.

Of more interest is the absorber response near perfect tuning. By inspection of Figure 4.7 it is clear that the absorber amplitudes are experiencing non-unison motion. However, when the experimentally obtained time traces for the two absorbers

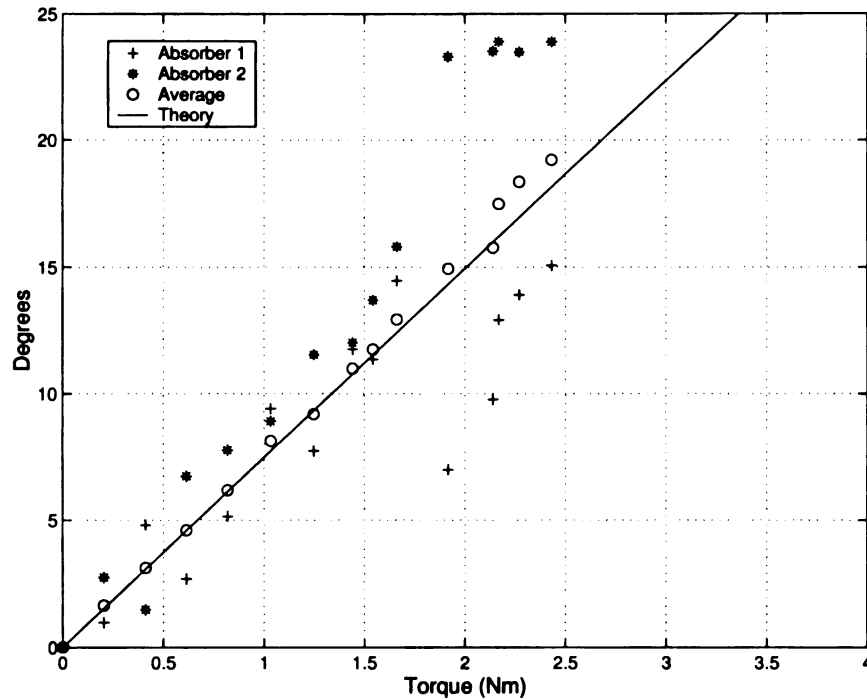


Figure 4.8. Absorber response at 0% mistuning showing deviation from unison response and the average response of both absorbers.

are averaged the resulting amplitudes fit the theoretical predictions, see Figure 4.8. The details of this are worthy of further comment. Consider the time histories of the absorber motion shown in Figure 4.9. Figure 4.9(a) shows the time trace for each absorber at $\hat{T}_\theta=1.03$ Nm. The relative phase difference between the two absorbers is found to be 61° and so the resulting average amplitude is less than either of the individual amplitudes. Indeed, it is very close to the theoretical prediction, see Figure 4.8.

Viewing Figures 4.9 more carefully, it is clear that a true steady-state response has not been reached. Although only 0.5 seconds of data are shown, the test was run for five minutes at each torque level prior to collecting data. Yet there is still a slight amplitude variation present. There are a number of possible reasons for

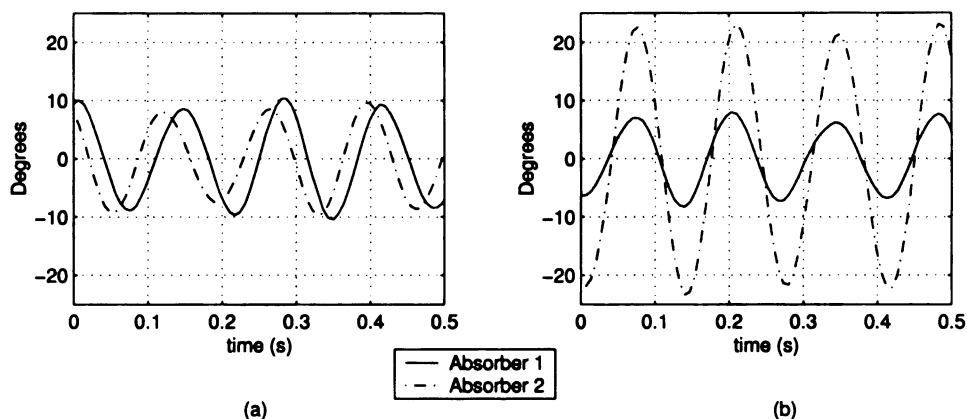


Figure 4.9. Time traces for two different \hat{T}_θ values from Figure 4.8 (0% mistuning)
(a) $\hat{T}_\theta=1.03$ Nm (b) $\hat{T}_\theta=1.92$ Nm.

this. Clearly a non-unison response is present and so from the analysis presented here, we cannot predict what the true response will be. However, it is likely to be very sensitive to small changes in the input parameters of the system, for example the mean speed, Ω . Very small changes in this may add transients to the responses that take a considerable time to decay. Alternatively, the responses observed may be the true post bifurcation responses that theory could predict. This is deserving of attention in future work.

Returning to Figure 4.9, a second pair of time responses are shown for a torque level of $\hat{T}_\theta=1.92$ Nm (Figure 4.9(b)). Here the relative phase difference between the two absorbers is found to be only 6° and so the average motion is very close to the average of the individual absorber amplitudes, i.e. mid-way between the values shown in Figure 4.8.

Finally, as shown in Figure 4.6, although there is close agreement between theoretical and experimental results in many cases the agreement is not so good as one approaches $n \simeq n_2$. The most likely reason for the discrepancy results is from the phase, ϕ , as defined in Equation 2.23. In addition to the reasons stated in the one

absorber case, the introduction of two absorbers is likely to make the system even more sensitive to small changes in the input parameters.

CHAPTER 5

Conclusion

It was the goal of this dissertation to explore the effects of mistuning on the performance of absorbers in a CPVA system riding on epicycloidal paths. The following will summarize the conclusions that are based on the findings of this dissertation.

- Introduction of more absorbers increases the effectiveness of the absorber system. As the number of absorbers increases, more inertia is made available to help absorb the fluctuating torque. Therefore, larger torque amplitudes may be applied to the system.
- Bifurcations to non-unison response were observed. In the two absorber case, small amounts of fluctuating torque would often result in the absorbers undergoing non-unison motion. This is especially true if operating close to perfect tuning.
- Generally there was excellent agreement between the theory and experimental results.

5.1 Future Work

Based on the successes encountered from the experiments conducted here, many possibilities are now open for exploration.

- Since bifurcations from the unison response were observed for all mistuning values, theoretical work should be extended on this behavior.
- Future tests should also measure the phases of each absorber. This would be useful for more detailed comparison with the theory - both for the unison and non-unison responses.
- The effects of subharmonic absorbers should be explored, i.e., absorbers tuned to $\frac{1}{2}$ the applied torque order.
- Effects of additional absorbers should also be explored to see their influence on reducing $|\ddot{\theta}|$ and study the bifurcations to the non-unison response.

BIBLIOGRAPHY

BIBLIOGRAPHY

- [1] V. Garg, *Effects of Mistuning on the Performance of Centrifugal Pendulum Vibration Absorbers*. MS Thesis, Michigan State University, 1996.
- [2] C.-P. Chao, *The Performance of Multiple Pendulum Vibration Absorbers Applied to Rotating Systems*. PhD Thesis, Michigan State University, 1997.
- [3] A. S. Alsuwaiyan, *Performance, Stability, and Localization of Systems of Vibration Absorbers*. PhD Thesis, Michigan State University, 1999.
- [4] T. Nester, *Experimental Approach to Centrifugal Pendulum Vibration Absorbers*. MS Thesis, Michigan State University, 2002.
- [5] H. H. Denman, "Remarks on brachistochrone-tautochrone problems," *American Journal of Physics*, vol. 53, pp. 781–782, 1985.

MICHIGAN STATE UNIVERSITY LIBRARIES



3 1293 02470 0027